Bioactive Materials 5 (2020) 832–843

Contents lists available at ScienceDirect

Bioactive Materials

journal homepage: http://www.keaipublishing.com/biomat

An all-silk-derived functional nanosphere matrix for sequential biomolecule delivery and *in situ* osteochondral regeneration

Wei Zhang[a,c,d,*], Chen Ling[b], Aini Zhang[a], Haoyang Liu[a], Yujie Jiang[a], Xiaolong Li[a], Renwang Sheng[a], Qingqiang Yao[b,d,**], Jialin Chen[a,c,d,***]

[a] School of Medicine, Southeast University, 210009, Nanjing, China
[b] Department of Orthopaedic Surgery, Institute of Digital Medicine, Nanjing First Hospital, Nanjing Medical University, 210006, Nanjing, China
[c] Jiangsu Key Laboratory for Biomaterials and Devices, Southeast University, 210096, Nanjing, China
[d] China Orthopedic Regenerative Medicine Group (CORMed), China

ARTICLE INFO

Keywords:
Osteochondral regeneration
Silk
Sequential delivery
BMSCs
Nanospheres

ABSTRACT

Endogenous repair of osteochondral defect is usually limited by the insufficient number of cells in the early stage and incomplete cell differentiation in the later stage. The development of drug delivery systems for sequential release of pro-migratory and pro-chondrogenic molecules to induce endogenous bone marrow-derived mesenchymal stem cells (BMSCs) recruitment and chondrogenic differentiation is highly desirable for *in situ* osteochondral regeneration. In this study, a novel, all-silk-derived sequential delivery system was fabricated by incorporating the tunable drug-loaded silk fibroin (SF) nanospheres into a SF porous matrix. The loading efficiency and release kinetics of biomolecules depended on the initial SF/polyvinyl alcohol (PVA) concentrations (0.2%, 1% and 5%) of the nanospheres, as well as the hydrophobicity of the loaded molecules, resulting in controllable and programmed delivery profiles. Our findings indicated that the 5% nanosphere-incorporated matrix showed a rapid release of E7 peptide during the first 120 h, whereas the 0.2% nanosphere-incorporated matrix provided a slow and sustained release of Kartogenin (KGN) longer than 30 days. During *in vitro* culture of BMSCs, this functional SF matrix incorporated with E7/KGN nanospheres showed good biocompatibility, as well as enhanced BMSCs migration and chondrogenic differentiation through the release of E7 and KGN. Furthermore, when implanted into rabbit osteochondral defect, the SF nanosphere matrix with sequential E7/KGN release promoted the regeneration of both cartilage and subchondral bone. This work not only provided a novel all-silk-derived drug delivery system for sequential release of molecules, but also a functional tissue-engineered scaffold for osteochondral regeneration.

1. Introduction

Articular cartilage defect is a common pathology of the knee joint and a leading cause of disability worldwide [1]. Physiologically, the articular cartilage is a transparent connective tissue covering the epiphyseal surface of the articulating bones, playing the role of reducing friction between adjacent bones. Articular cartilage is devoid of blood vessels, nerves, and lymphatics, and has limited self-repair capacity [2]. Often, damage to the chondral region extends to the underlying subchondral bone, leading to progressive total joint destruction (defined as osteochondral defect) [3]. The management of osteochondral defects is one of the most challenging clinical problems due to the distinct physiochemical and biological properties of cartilage and subchondral bone [4]. Although there has been some success, current treatments including subchondral drilling, microfracture and osteochondral autologous/allograft transplantation are limited by the lack of available tissue, donor site morbidity, mechanical inferiority and host immune reactions [2,4]. Hence, the ongoing search for appropriate treatment methods is necessary to enhance osteochondral regeneration.

Recently, *in situ* tissue engineering provides a promising strategy via motivating endogenous bone marrow-derived mesenchymal stem cells (BMSCs) for osteochondral repair [5–7]. The repair process through

Peer review under responsibility of KeAi Communications Co., Ltd.
* Corresponding author. School of Medicine, Southeast University, 210009, Nanjing, China.
** Corresponding author. Department of Orthopaedic Surgery, Institute of Digital Medicine, Nanjing First Hospital, Nanjing Medical University, 210006, Nanjing, China.
*** Corresponding author. School of Medicine, Southeast University, 210009, Nanjing, China.
E-mail addresses: zhang.wei@seu.edu.cn (W. Zhang), yaoqingqiang@njmu.edu.cn (Q. Yao), jialin.chen@seu.edu.cn (J. Chen).

https://doi.org/10.1016/j.bioactmat.2020.05.003
Received 26 February 2020; Received in revised form 23 May 2020; Accepted 23 May 2020

endogenous BMSCs is typically initiated by the earliest response of BMSCs migration to the defect site, and followed by the process of BMSCs differentiation to the specific lineages [8,9]. Biomaterials play a significantly important role as to provide physical protection and to present biochemical cues to activate the intrinsic regenerative capacity of BMSCs [10,11]. A broad spectrum of tissue-engineered scaffolds has been developed for the delivery of pro-migratory and pro-differentiation molecules to improve endogenous osteochondral regeneration via BMSCs [12–14]. Recently, there has been growing evidence that sequential presentation of inductive molecules to coordinate the tissue repair cascade response would further improve the repair efficacy [15–18]. Shen et al. reported that the rapid initial release of pro-migratory stromal cell-derived factor 1 (SDF-1) and the subsequent slow and sustained release of bone morphogenetic protein 2 (BMP-2) significantly enhanced bone regeneration compared to the simultaneous release of both biomolecules [18]. Directional recruitment of BMSCs into the defect area in the early stage is a prerequisite for subsequent BMSCs chondrogenic differentiation, and ultimately osteochondral regeneration [9]. A variety of natural and synthetic materials have been explored for the development of sequential biomolecule delivery systems. The conventional strategy is to load different biomolecules on different kinds of biomaterials [17,19,20]. These multi-material-based systems can sequentially release multiple factors due to the different degradability, hydrophobicity, or surface charge of respective material fractions [19,20]. However, these systems often require complicated material compositions, complexed fabrication procedures, and toxic chemical reagents, which may damage the biomolecule bioactivity and limit their clinical translation [17,19–21]. In light of this, there is a great need for the preparation of sequential biomolecule delivery systems using simple, rapid and green-chemistry techniques.

Silk fibroin (SF), derived from the *Bombyx mori* (*B. mori*) silkworm, is a U.S. Food and Drug Administration (FDA) approved biomaterial for clinical use. SF has been widely used in tissue engineering applications due to its good biocompatibility, controllable degradability, robust mechanical properties, and non-inflammatory byproducts [22,23]. Along with these attractive material properties, SF provides a versatile biomaterial platform to be processed into different material formats, including spheres, sponges, hydrogels, and films, etc [15,24,25]. SF spheres have been explored as an effective carrier for the delivery of both hydrophilic and hydrophobic molecules due to the amphiphilic nature [18,26,27]. Wang et al. demonstrated that SF micro/nanospheres, prepared through the phase separation method, have tunable drug loading and release properties by changing the concentration, molecular weight or ratios between different polymers [27]. The entire fabrication process is performed under simple, mild, and aqueous conditions [27]. According to these characteristics, it is speculated that SF nanospheres can be explored as a sequential biomolecule delivery system by simply adjusting the nanosphere properties. However, previous studies have not systematically investigated the potential of SF nanosphere-based delivery systems for sequential release of multiple molecules, nor the application of such systems to enhance the *in vivo* regenerative process of osteochondral defects.

In this study, we aimed to develop an all-silk-derived sequential biomolecule delivery system to initially promote BMSCs migration via the delivery of pro-migratory molecule and then to enhance BMSCs chondrogenesis through the subsequent sustained release of pro-chondrogenic molecule for effective osteochondral regeneration (Scheme 1). This programmed delivery system consisted of a SF porous matrix incorporated with the tunable SF nanospheres that encapsulate BMSC affinity peptide E7 and chondrogenic molecule Kartogenin (KGN), respectively. E7 is a recently-identified 7-amino acid (EPLQLKM) small peptide. E7 was chosen because it has a high specific affinity to BMSCs and has been reported to improve BMSCs adhesion, proliferation and migration both *in vitro* and *in vivo* [28–33]. KGN is a well-recognized small molecule that can induce MSCs chondrogenesis and promote cartilage repair without the disadvantages of growth factors such as immunogenicity, instability, and short half-life [34–37]. The loading efficiency and release kinetics of the biomolecules depended on the initial SF/polyvinyl alcohol (PVA) concentrations (0.2%, 1% and 5%) of the nanospheres, as well as the hydrophobicity of the loaded molecules, resulting in controllable and programmed delivery profiles. The prepared SF nanosphere matrix showed a rapid initial release of E7 peptide with 5% nanospheres during the first few days, and subsequently a slow and sustained release of KGN with 0.2% nanospheres longer than 30 days. Our results demonstrated that the programmed release of E7 and KGN from the SF nanosphere matrix effectively promoted the regeneration of cartilage and subchondral bone in rabbit osteochondral defect model.

2. Materials and methods

2.1. Preparation of SF solution

SF solution was prepared as previously reported [24]. In brief, raw silk fibers (*Bombyx mori*, Zhejiang Xingyue Biotechnology, Hangzhou, China) were boiled in 0.02 M Na_2CO_3 for half an hour and then dissolved in 9.3 M LiBr for 4 h at 60 °C. After dialysis against ultrapure water for 48 h, the solution was centrifugated twice at 9000 r.p.m at 4 °C for 20 min, and the supernatant was collected and stored at 4 °C before use.

2.2. Preparation of SF nanospheres

SF nanospheres were prepared through phase separation between SF and PVA (Macklin, Shanghai, China) [24,27]. In brief, SF solution and PVA solution with the same initial concentration (0.2%, 1% and 5%) was mixed with the volume ratio of 1/4. To fabricate the drug-loaded nanospheres, 100 μg/ml E7 peptide (EPLQLKM, Scilight-Peptide, Beijing, China), 1 μg/ml FITC-labeled E7 (Scilight-Peptide, Beijing, China), 10 μM KGN (Sigma-Aldrich, St Louis, MO, USA) or 1 μg/ml Rhodamine B (RhoB, Macklin, Shanghai, China) were added to the solution. The blend solution was sonicated with an X0-400S ultrasonic processer (Atpio Co., Nanjing, China) at 25% amplitude for 30 s. The solution was poured into a petri dish to evenly cover the bottom of the dish, and was dried overnight in fume hood. The dried film was dissolved in ultrapure water under shaking for 30 min and centrifuged at 11000 r.p.m. at 4 °C for 20 min, to remove the residual PVA from the SF spheres. The supernatant was collected for the measurement of drug loading efficiency. After removing the supernatant, the pellet was suspended in ultrapure water to obtain the SF nanosphere suspension.

2.3. Preparation of SF nanosphere matrix

SF nanosphere suspension was mixed with 6% SF solution with the volume ratio of 1/3. The mixture was frozen at −80 °C overnight and lyophilized for 24 h in a FD-1A-50 freeze dryer (Boyikang, Beijing, China). Then the scaffold was treated with 90% methanol (Sinopharm, Shanghai, China) for 1 h to induce crosslinking. After re-lyophilization, the scaffold was cut into the required size using a biopsy punch. The SF porous matrix without nanosphere incorporation is termed as PM, and the SF porous matrix incorporated with 0.2%, 1% or 5% nanospheres is termed as 0.2%NS-PM, 1%NS-PM or 5%NS-PM, respectively. The unloaded, E7-loaded, KGN-loaded or E7/KGN-loaded SF nanosphere matrix is termed as NS-PM, E7@NS-PM, KGN@NS-PM or E7/KGN@NS-PM, respectively.

2.4. Scanning electron microscope (SEM) imaging

After being freeze-dried and sputter coated with gold, the SF nanospheres and SF nanosphere matrices were observed by using a Zeiss EVO 18 SEM (Carl-Zeiss, Oberkochen, Germany) to evaluate the surface structure of the sample.

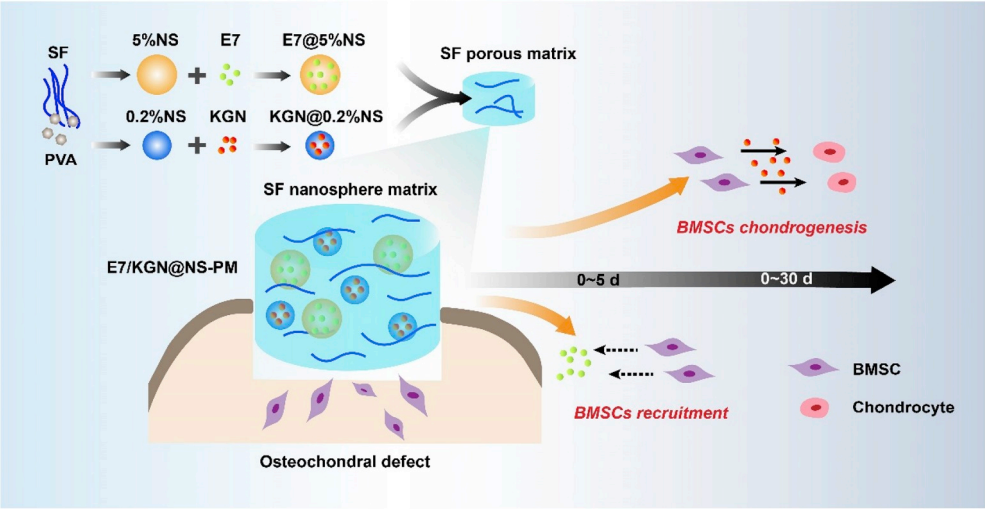

Scheme 1. Overview of SF nanosphere matrix with sequential E7/KGN release in osteochondral defect repair.

2.5. Dynamic light scattering (DLS) measurement

The hydrodynamic size and surface zeta potential of the SF nanospheres was determined using DLS technique with a Zetasizer Nano S90 (Malvern, Worcestershire, UK).

2.6. Mechanical evaluation

An electric universal testing machine (UTM2502; Sunstest, Shenzhen, China) was used to measure the compressive mechanical properties of the scaffolds (diameter: 14 mm, height: 6 mm). Sensor of 500 N and crosshead speed of 4.8 mm/min was used. The compressive modulus of the tested scaffold was calculated from the linear region of the stress-strain curve.

2.7. Swelling ratio

The swelling ratio of the scaffolds was estimated using the gravimetric method as previously [12]. The dry weight of scaffolds (M0) was determined at the beginning of the assay. After that, scaffolds were incubated in PBS at 37 ˚C. At the time point of 1, 8, 24 and 48 h after incubation, the wet weight of the scaffolds (M1) was measured. The swelling ratio was calculated as follow:

$$\text{Swelling ratio} = (M1\text{-}M0)/M0$$

2.8. In vitro degradation

The dry weight of the scaffolds (M0) was determined at the beginning of the assay. Subsequently, scaffolds were incubated in PBS at 37 ˚C with shaking. At the designated time-points, the scaffolds were washed, dried, and weighed (M1). The weight remaining was calculated using the equation below:

$$\text{Weight remaining (\%)} = M1/M0*100$$

2.9. Controlled release profile

Scaffolds were incubated in PBS at 37 ˚C with shaking. At the designated time-points, supernatant fluid was collected for analysis, and fresh PBS was refilled. The measurement of cumulative release of molecules was performed on a Synergy H1 microplate reader (BioTek, Winooski, VT, USA). FITC-labeled E7 was measured at 488/519 nm, RhoB was measured at 550/620 nm, and KGN was measured at 278 nm.

2.10. Cell culture

Primary rat BMSCs (Cyagen Biosciences, Suzhou, China) were cultured in low glucose DMEM (Gibco, Carlsbad, CA, USA) supplemented with 10% fetal bovine serum (FBS, Wisent, Canada) and 1% penicillin-streptomycin (Gibco, Carlsbad, CA, USA). Medium was changed every 3rd day until the cells reached 80%–90% confluence.

2.11. Cell proliferation

BMSCs were seeded on SF nanosphere matrix and cultured for 1, 3 and 5 days. The cell-seeded scaffold was washed with PBS, transferred to a new well, and incubated in 10% CCK-8 solution (NCM Biotech, Suzhou, China) at 37 ˚C for 1 h. The absorbance was measured using an 800 TS microplate reader (BioTek, Winooski, VT, USA) at 450 nm.

2.12. Cell viability

BMSCs were seeded on SF nanosphere matrix and cultured for 3 days. The cell-seeded scaffold was washed with PBS, transferred to a new well, and stained with DAPI (Beyotime, Shanghai, China) or Calcein-AM/PI Double Staining Kit (Dojindo, Japan). The cells were observed using an EVOS FL Auto 2 Cell Imaging System (Invitrogen, Carlsbad, CA, USA).

2.13. Cell migration

BMSCs were pre-stained with Dil (Beyotime, Shanghai, China) before being seeded into 24-well plate. A scratch in a confluent monolayer of BMSCs was performed by using a 200 μl tip in the center of the well. Subsequently, SF nanosphere matrix was placed into a 0.4 μm transwell insert (NEST Biotechnology, China), which was placed in each well of the 24-well plate. 1 ml serum-free DMEM was added into each well. Pictures of cells at 0 and 24 h were captured. The migration area was quantified using ImageJ software (NIH, Bethesda, MD, USA).

2.14. Chondrogenic differentiation

BMSCs were seeded on SF nanosphere matrix and cultured in MesenCult™-ACF Chondrogenic Differentiation Kit (STEMCELL Technologies, Canada) for 14 days. The medium was changed every other day. Positive induction of chondrogenesis was confirmed by Alcian Blue staining (1%, pH = 2.5, Macklin, China) for glycosaminoglycan (GAG) deposition. Then the staining was solubilized with 6 M

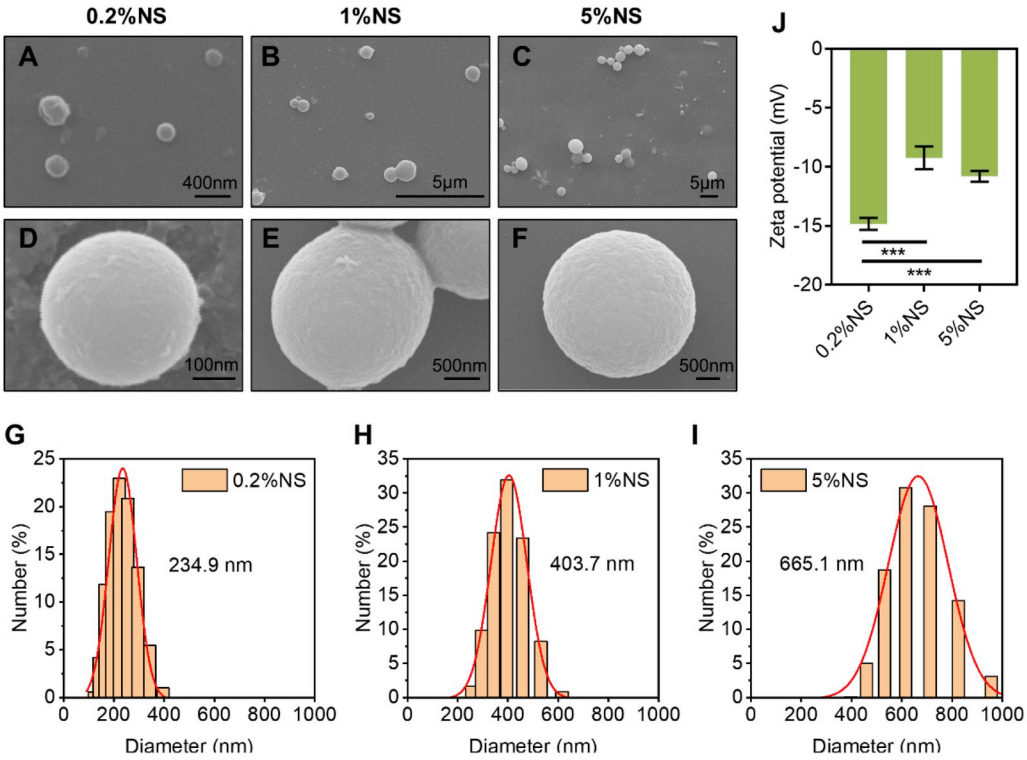

Fig. 1. SEM images of SF nanospheres fabricated from 0.2% (A, D), 1% (B, E) and 5% (C, F) SF/PVA concentrations. Scale bars = 400 nm in (A), 5 μm in (B, C), 100 nm in (D), and 500 nm in (E, F). DLS measurements for SF nanospheres fabricated from 0.2% (G), 1% (H) and 5% (I) SF/PVA concentrations. (J) Zeta potential of SF nanospheres. ***P < 0.001.

Guanidine-HCl (Aladdin, Shanghai, China) and the absorbance was measured at 630 nm on a Synergy H1 microplate reader (BioTek, Winooski, VT, USA).

2.15. Animal model

The study protocol was approved by the Animal Experimental Ethical Inspection Committee of Southeast University. Adult male New Zealand white rabbits (~2.5 kg) were used in this study. Osteochondral cylindrical defects (diameter: 4 mm, height: 3.5 mm) were created on the patellar groove, and then implanted with the unloaded (NS-PM, n = 4), E7-loaded (E7@NS-PM, n = 4), KGN-loaded (KGN@NS-PM, n = 4) or E7/KGN-loaded (E7/KGN@NS-PM, n = 4) SF nanosphere matrices. After surgery, rabbits were allowed to move freely and fed with standard food and water. All the animals were sacrificed at 12 weeks post-operation.

2.16. Micro-CT evaluation

Samples were scanned and imaged by using a Micro-CT scanner (Inveon PET/CT, Siemens, Germany). Reconstruction and data analysis were performed using the Mimics software (Materialise, Belgium), including bone volume/total volume (BV/TV), trabecular thickness (Tb.Th) and trabecular numbers (Tb.N). A cylindrical region of interest (ROI, diameter: 4 mm, height: 4 mm) was concentrically positioned over the defect site with the threshold between 350 and 1080 for cartilage analysis, and higher than 1080 for bone analysis.

2.17. Macroscopic and histological assessment

Samples were examined and photographed with a stereo-microscope (SZ61, Olympus, Japan) for macroscopic evaluation according to the International Cartilage Repair Society (ICRS) macroscopic assessment scale (Table S1) [38]. As for histological assessment, samples were fixed in 4% paraformaldehyde, and then decalcified in 10% EDTA for 4 weeks under gentle shaking. The decalcified samples were embedded and sectioned. Hematoxylin and eosin (H&E) staining and Safranine-O staining were performed for tissue morphological evaluation and GAG distribution analysis. Histological evaluation for the overall defect, the chondral (within the upper 1 mm of the defect) and subchondral (within the bottom 2 mm of the defect) regions was performed based on an established histological scoring system (Table S2) [39]. Immunohistochemical staining for Aggrecan (Proteintech, China), Collagen I (Proteintech, China) and CD44 (Proteintech, China) was performed to evaluate the expression of cartilage marker, fibrocartilage marker and BMSCs marker, respectively.

2.18. Statistics

Student's t-test was used for statistical analysis when comparing two groups. One-way ANOVA with Tukey's multiple comparisons was performed when comparing between more than two groups. Statistical differences were considered significant at a P-value of < 0.05.

3. Results and discussion

3.1. Fabrication and characterization of SF nanospheres with tunable properties

SF nanospheres were fabricated by a simple, rapid and green-chemistry method by phase separation between PVA and SF with the same concentrations [24,27]. The only chemical used is PVA, an FDA-approved pharmaceutical ingredient that is ultimately removed from the SF nanospheres by centrifugation [27]. Under SEM, the SF nanospheres fabricated from 0.2%, 1% and 5% SF/PVA concentrations showed a spherical shape and smooth surface, and their sizes ranged from about 200 nm to few micrometers (Fig. 1A–F). The spheres increase in size as the initial silk/PVA concentrations increases during SF sphere preparation. DLS measurements revealed that the average hydrodynamic diameter of 234.9 nm for the 0.2% nanospheres, 403.7 nm for the 1% nanospheres, and 665.1 nm for the 5% nanospheres (Fig. 1G–I). The 0.2% nanospheres showed more homogeneous size distribution as compared to the 1% and 5% nanospheres (Fig. 1G–I). The surface zeta potential for the 0.2% nanospheres (−14.8 mV) was

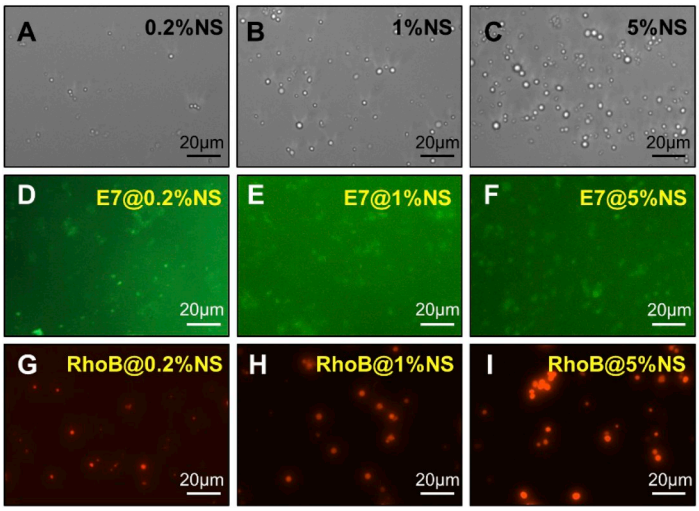

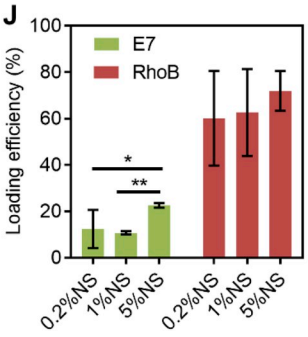

	Property	M.W.
E7	Hydrophilic	858
KGN	Hydrophobic	317
RhoB	Hydrophobic	479

Fig. 2. (A-C) Unloaded SF nanospheres under light microscope. Scale bars = 20 μm. (D-F) SF nanospheres encapsulated with FITC-labeled E7 under fluorescence microscope. Scale bars = 20 μm. (G-I) SF nanospheres encapsulated with RhoB under fluorescence microscope. Scale bars = 20 μm. (J) Loading efficiency of E7 and RhoB in SF nanospheres. The table shows the properties of the molecules. *P < 0.05, **P < 0.01.

more negative than that of the 1% (−9.2 mV) and 5% SF nanospheres (−10.8 mV) (Fig. 1J).

The prepared SF nanospheres were used for the encapsulation of BMSC affinity peptide E7 and chondrogenic molecule KGN, which have been reported to stimulate the recruitment and chondrogenic differentiation of BMSCs respectively [28,33,35,40]. E7 is a 7-amino acid (EPLQLKM), hydrophilic small peptide (M.W. 858 g/mol), while KGN is an extremely hydrophobic small molecule (M.W. 317 g/mol) [29,41]. SF molecule have been identified with characteristic amphiphilic nature, thereby facilitating the loading of both hydrophilic and hydrophobic molecules in SF nanospheres [27]. Unloaded nanospheres could be observed under light microscope (Fig. 2A–C). Weak green fluorescence was observed from the SF nanospheres encapsulated with FITC-labeled E7, indicative of successful loading of E7 peptide on the nanospheres (Fig. 2D–F). The loading efficiency of E7 for the 5% nanospheres was approximately 22.6%, significantly higher than that of the 0.2% nanospheres (12.4%) and the 1% nanospheres (10.7%) (Fig. 2J). To monitor the loading of hydrophobic small molecule, RhoB (M.W. 479 g/mol) was encapsulated in the SF nanospheres as a model molecule because it can emit red fluorescence after excitation. RhoB-loaded nanospheres showed stronger red fluorescence as compared to the E7-loaded nanospheres (Fig. 2G–I). A high loading efficiency of > 60% was measured for the RhoB-loaded nanospheres irrespective of SF/PVA concentrations (Fig. 2J). The hydrophilicity of the E7 peptide apparently determines its low binding affinity to SF, while the hydrophobic interactions between RhoB and SF lead to higher binding than that of E7. This is consistent with the previous report that the loading efficiency of the hydrophilic molecule (tetramethylrhodamine conjugated dextran) in SF spheres was significantly lower than that of the hydrophobic molecules (RhoB or tetramethylrhodamine conjugated bovine serum albumin) [27].

3.2. SF matrix incorporated with tunable nanospheres mediates programmed release of biomolecules

The molecule-loaded SF nanospheres were subsequently incorporated into a SF porous scaffold to prepare an all-silk-derived drug release system. Under SEM, SF porous matrix (PM) showed a smooth surface (Fig. 3A), while the 0.2% nanosphere-incorporated matrix (0.2%NS-PM) showed a rough and nanoparticulate surface (Fig. 3B). SF nanospheres were more obviously identified in matrices incorporating 1% and 5% nanospheres (1%NS-PM, Fig. 3C; 5%NS-PM, Fig. 3D). The incorporation of nanospheres did not significantly altered the compressive modulus of the porous scaffolds, regardless of the size of the spheres (Fig. 3E). However, the swelling ratio of the 1%NS-PM and 5% NS-PM matrices was significantly higher than those of the PM group (1, 8, 24 and 48 h) and the 0.2%NS-PM group (24 h), suggesting higher water absorption ability (Fig. 3F). When incubated in PBS at 37 °C, different SF nanosphere-incorporated matrices (0.2%NS-PM, 1%NS-PM and 5%NS-PM) showed comparable degradation curves with a mass loss of about 15% in 37 days, which were significantly faster than that of the pure SF matrix (PM, 3.54% mass loss) (Fig. 4A).

Next, we investigated the release profiles of hydrophilic and hydrophobic molecules from the SF nanosphere matrix. The matrix incorporated with different SF nanospheres showed distinct release profiles of the hydrophilic E7 peptide (Fig. 4B). The 5%NS-PM matrix released the loaded E7 more rapidly than the 0.2%NS-PM and 1%NS-PM matrices, with approximately 4-fold released E7 within 120 h (Fig. 4B). The faster release of E7 from the 5%NS-PM matrix was mainly attributed to the higher E7 loading efficiency and higher swelling ratio of the 5%NS-PM matrix, since a high degree of swelling due to water uptake would increase the released amount of hydrophilic drugs [42]. In contrast, the release curves of the hydrophobic molecules in different matrices showed similar and sustained trends. Both KGN and RhoB were released from the matrices more continuously at an almost constant rate (Fig. 4C and D). This is because hydrophobic molecules have a stronger binding to silk through hydrophobic interactions, and therefore have higher loading efficiency and slower release kinetics than hydrophilic molecules [27]. Among the 3 different matrices, the 0.2%NS-PM showed a more sustained release of both KGN and RhoB, as compared to the 1%NS-PM and 5% NS-PM (Fig. 4C and D). We speculate that the more negative zeta potential of the 0.2% nanospheres (−14.8 mV) might contribute to the stronger binding of RhoB (positive charge) to SF nanospheres via electrostatic attraction, resulting in a slower release profile than the 1% or 5% nanospheres. Taken together, the release profiles of the biomolecules from the SF nanosphere matrix could be tuned to the desired rate by changing the initial SF/PVA concentrations of the nanospheres, resulting in controllable and programmed delivery profiles.

The directional migration of endogenous BMSCs to the defect site at early stage, followed by directed differentiation of BMSCs towards chondrogenic lineages are integral for efficient osteochondral regeneration. Our findings indicated that the 5% nanosphere-incorporated matrix showed a rapid release of E7 peptide during the first 120 h, whereas the 0.2% nanosphere-incorporated matrix provided a slow and sustained release of KGN longer than 30 days. Though the endogenous repair of osteochondral defects differs from the size of the defects, studies have recognized three typical stages of the repair cascade in rabbit osteochondral model: 1) fibrin clot formation between days 3 and 7 post-injury, 2) onset of cartilage repair between days 7 and

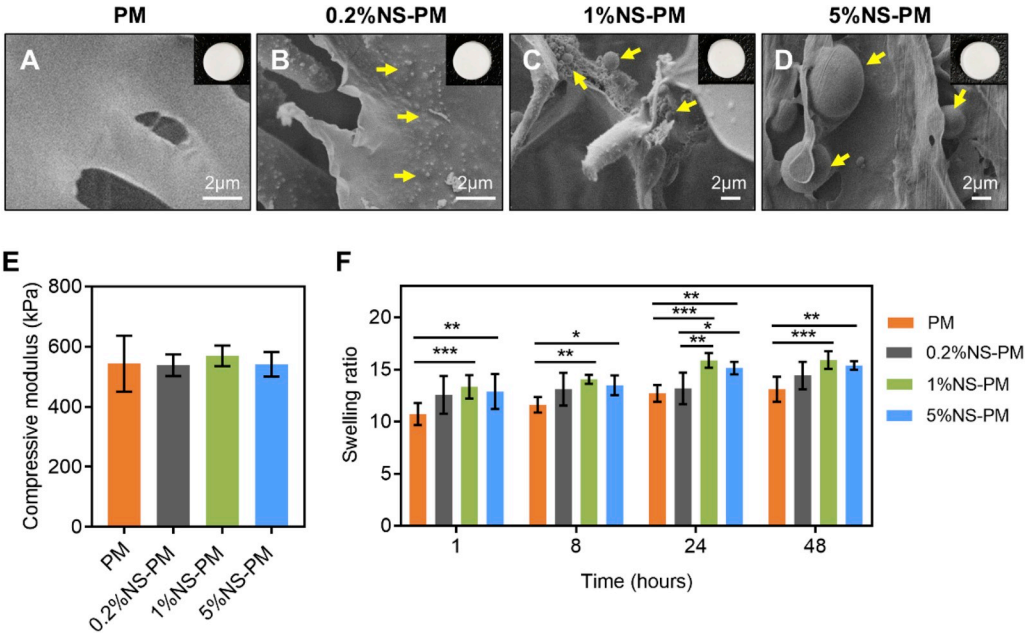

Fig. 3. (A-D) SEM images of SF porous matrix incorporated with different SF nanospheres. Inserts are the gross morphology of the matrices. The arrows indicate the incorporated nanospheres. Scale bars = 2 μm. (E) Compressive modulus of SF nanosphere matrices. (F) Swelling ratio of SF nanosphere matrices after being incubated in PBS for 1, 8, 24 and 48 h *P < 0.05, **P < 0.01, ***P < 0.001.

14 post-injury, and 3) onset of intramembranous and/or endochondral bone formation between days 21 and 28 post-injury [43]. Therefore, we consider that the sequential release of E7 from 5% nanospheres following by KGN from 0.2% nanospheres could potentially direct the coordinated phases of osteochondral regeneration by facilitating BMSCs recruitment and chondrogenesis. Notably, the programmed release profiles of pro-migratory and pro-differentiation molecules in this current work are basically consistent with the previous report, which have been proven effective for bone regeneration [18]. In light of these data, we fabricated the SF nanosphere matrix with sequential E7/KGN release employing the 5% nanospheres for the encapsulation of E7, and the 0.2% nanospheres for the encapsulation of KGN, for the following experiments.

3.3. SF nanosphere matrix with sequential E7/KGN release enhances BMSCs migration and chondrogenic differentiation in vitro

We next evaluated the biocompatibility and biofunctionality of the SF nanosphere matrices on *in vitro* cultured BMSCs. CCK-8 analysis showed that the cell proliferation rates increased over time on SF nanosphere matrices with or without biomolecule loading (Fig. 5A). BMSCs were able to adhere and grow on the matrices, as evidenced by the DAPI staining (Fig. 5B) and the Live/dead staining (Fig. 5C, Fig. S1) after 3 days of culture, indicating good biocompatibility of the SF nanosphere matrices.

Since BMSC affinity peptide E7 is a recognized biomolecule which can target BMSCs recruitment and promote BMSCs adhesion

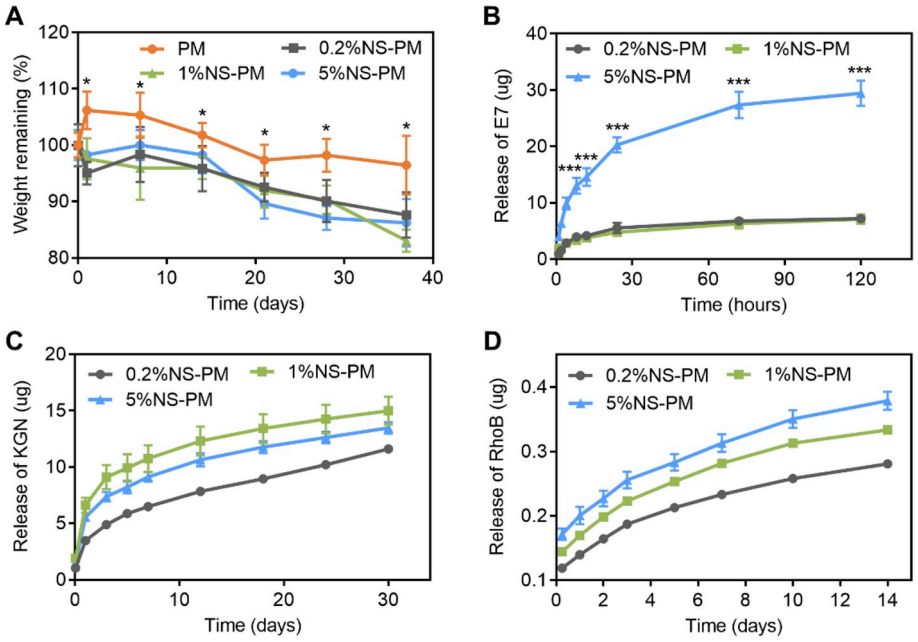

Fig. 4. (A) *In vitro* degradation curves of SF nanosphere matrices in PBS at 37 °C. (B) Cumulative E7 release from SF nanosphere matrices at 37 °C. (C) Cumulative KGN release from SF nanosphere matrices at 37 °C. (D) Cumulative RhoB release from SF nanosphere matrices at 37 °C. *P < 0.05, ***P < 0.001.

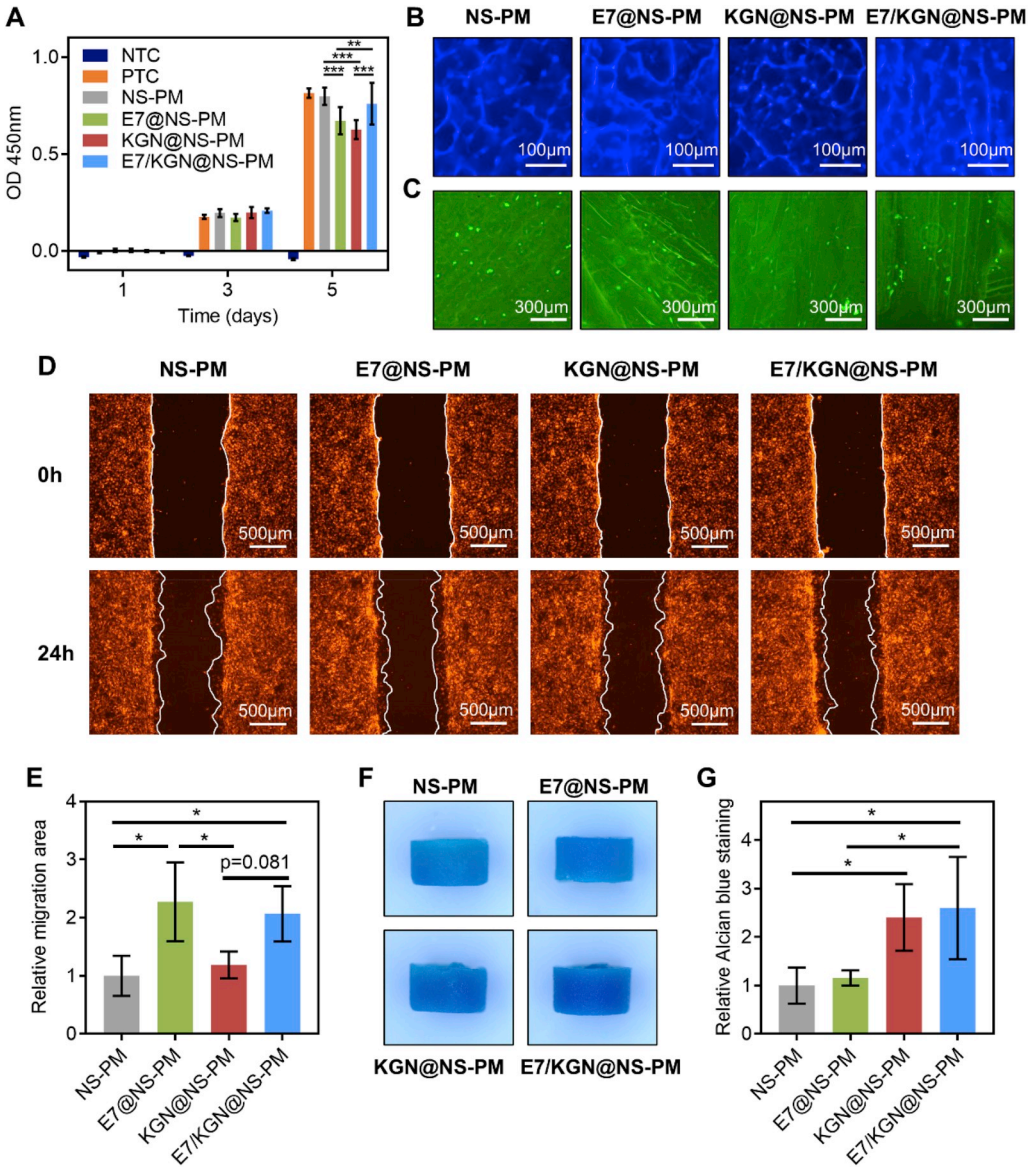

Fig. 5. (A) The proliferation of BMSCs cultured on SF nanosphere matrices measured by CCK-8 at 1, 3, and 5 days. NTC: negative control, 5% DMSO; PTC: positive control, normal culture medium. (B) DAPI staining of BMSCs after 3 days of culture on SF nanosphere matrices. Scale bars = 100 μm. (C) Live/dead staining of BMSCs after 3 days of culture on SF nanosphere matrices. The superimposed image shows both Calcein AM (green, live) and PI (red, dead) staining. Scale bars = 300 μm. (D) BMSCs migration exposed to different SF nanosphere matrices examined by the *in vitro* scratch assay. Cells were pre-stained with Dil. The white lines indicate cell migration fronts. Scale bars = 500 μm. (E) Quantification of the relative migration area. The migration area in the NS-PM group was set as 1. (F) Alcian blue staining of BMSCs-seeded SF nanosphere matrices after 14 days of culture in chondrogenic medium. (G) Quantification of Alcian blue staining by measuring the absorbance of the eluent at 630 nm. The staining intensity in the NS-PM group was set as 1.*P < 0.05, **P < 0.01, ***P < 0.001.

[28–30,33], the nanosphere matrices with E7 incorporation (E7@NS-PM, E7/KGN@NS-PM) enhanced BMSCs migration compared to the unloaded matrix (NS-PM) or the KGN-loaded matrix (KGN@NS-PM) as evidenced by the *in vitro* scratch assay (Fig. 5D and E). KGN is a well-identified small molecule that can induce the selective differentiation of MSCs into chondrocytes [34–36]. BMSCs-seeded SF nanosphere matrices were cultured in chondrogenic medium for 14 days and stained with Alcian blue for the evaluation of GAG deposition. The KGN-loaded matrices (KGN@NS-PM, E7/KGN@NS-PM) showed more intensive staining than the NS-PM and E7@NS-PM matrices (Fig. 5F). Further quantification of Alcian blue staining by measuring the absorbance of the eluent at 630 nm revealed that the KGN@NS-PM and E7/KGN@NS-PM groups displayed more than 2-fold GAG synthesis as compared to the NS-PM and E7@NS-PM groups (Fig. 5G).

3.4. SF nanosphere matrix with sequential E7/KGN release promotes osteochondral regeneration in vivo

We further investigated the therapeutic efficacy of the SF nanosphere matrices on *in situ* osteochondral repair. The unloaded (NS-PM), E7-loaded (E7@NS-PM), KGN-loaded (KGN@NS-PM) or E7/KGN-loaded (E7/KGN@NS-PM) nanosphere matrices were implanted into rabbit osteochondral defects on patellar groove, respectively. After 12 weeks, macroscopic images reveled that the cartilage surfaces of the NS-PM (Fig. 6A and E) and KGN@NS-PM (Fig. 6C and G) groups was not fully repaired, and there were large defects in the central region. In contrast, a fully-filled, white and well-integrated regenerated cartilage tissue was found in the E7/KGN@NS-PM group (Fig. 6D and H). In the E7@NS-PM group, the defect was almost completely repaired, but a small hole remained in the center of the newly-formed tissue (Fig. 6B and F). Subsequent measurements of the repaired tissue area further confirmed this observation. Defects treated with E7/KGN@NS-PM matrix showed the highest repair efficacy, with an average repaired tissue area ratio of 89%, which was higher than that of the NS-PM (68%), E7@NS-PM (87%) and KGN@NS-PM (64%) matrices (Fig. 6I). Additionally, according to the ICRS repair assessment for macroscopic observations, the overall scores of the E7@NS-PM and E7/KGN@NS-PM groups were significantly higher than those of other groups (Fig. 6J).

3D reconstruction from Micro-CT images revealed that in the subchondral bone area, in contrast to the small amount of calcified tissue in the NS-PM (Fig. 7A and E), E7@NS-PM (Fig. 7B and F) and KGN@NS-PM (Fig. 7C and G) groups, a large amount of newly-formed bone tissue was found in the E7/KGN@NS-PM group (Fig. 7D and H). Fig. 7I–K

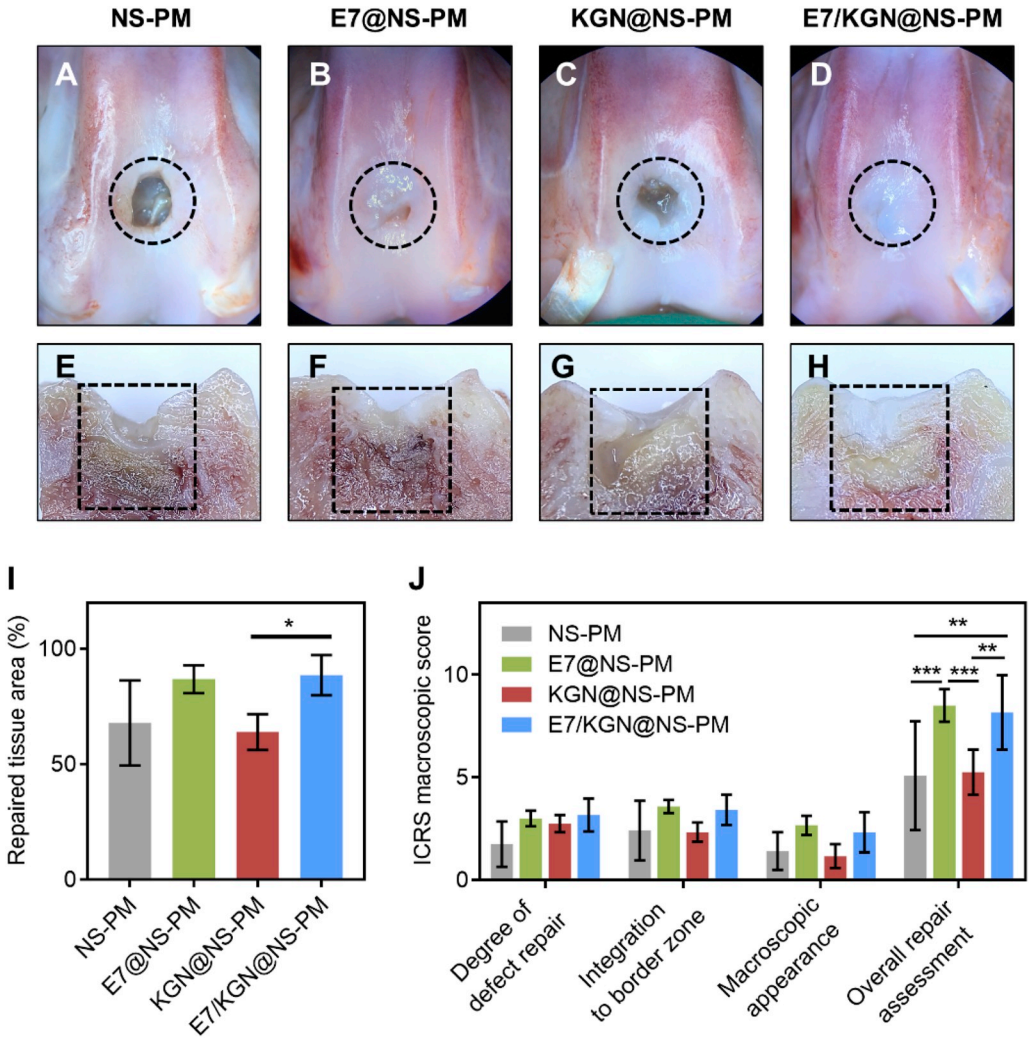

Fig. 6. (A-D) Gross morphology of joint samples harvested at 12 weeks post-operation. The black circles indicate the original defect borders. (E-H) Sagittal views of osteochondral defects at 12 weeks post-operation. The black boxes indicate the original defect borders. (I) Quantitative analysis of the repaired tissue area per total defect area (%). (J) Macroscopic evaluation according to the ICRS macroscopic scores. *P < 0.05, **P < 0.01, ***P < 0.001.

showed the quantification of bone formation by BV/TV, Tb.Th and Tb.N. For all measured parameters, the E7/KGN@NS-PM group had the highest values, while the NS-PM group had the lowest values among the 4 groups. In addition, the calculated BV/TV and Tb.Th of the E7/KGN@NS-PM group were significantly higher than those of the NS-PM group (Fig. 7I–K).

Histological analysis for osteochondral defect repair at 12 weeks post-implantation was further performed using the H&E and Safranin-O staining. In the NS-PM and KGN@NS-PM groups, the defects were not adequately repaired with only a small amount of fibrous tissue filled the defect area, leaving large residual void spaces in the center (Fig. 8A, 8C, 8E, 8G). The defects in the E7@NS-PM group were filled with a certain amount of loosely arranged, weakly stained fibrous tissue in both the cartilage and the subchondral area (Fig. 8B and F). In clear contrast, the E7/KGN@NS-PM group displayed enhanced regeneration of both cartilage and subchondral bone. The osteochondral defect was almost covered by abundant hyaline cartilage-like tissue that was well-integrated with the surrounding tissue (Fig. 8D and H). Consistent with this observation, the E7/KGN@NS-PM group showed the highest histological total score, cartilage sub-score and subchondral bone sub-score among the 4 groups, which were significantly higher than those of the NS-PM group (Fig. 8I–K).

At 12 weeks post-implantation, immunohistochemical staining displayed a more intense Aggrecan staining in the repaired tissue from the E7/KGN@NS-PM group, as compared to the other groups (Fig. 9A–D). Immunohistochemical staining of fibrocartilage marker Collagen I showed that the neo-tissue in the cartilage area was weakly positive in the NS-PM, E7@NS-PM and KGN@NS-PM groups, but negative in the E7/KGN@NS-PM group (Fig. 9E–H). It indicated that the E7/KGN@NS-PM matrix promoted cartilage repair without fibrocartilage remodeling. The repaired tissue in the E7@NS-PM and E7/KGN@NS-PM groups displayed higher proportion of CD44-positive cells as compared to the NS-PM and KGN@NS-PM groups, indicating that the E7-loaded matrices could more efficiently recruit endogenous BMSCs from the bone marrow (Fig. 10A–D). These findings are consistent with the previous reports that E7-conjugated PCL meshes could selectively capture CD44-, CD90-, and CD105-positive BMSCs both *in vitro* and *in vivo* [30].

The endogenous repair efficacy of osteochondral defect is limited in part by the insufficient number of cells in the early stage and the incomplete cell differentiation in the later stage. The rapid release of pro-

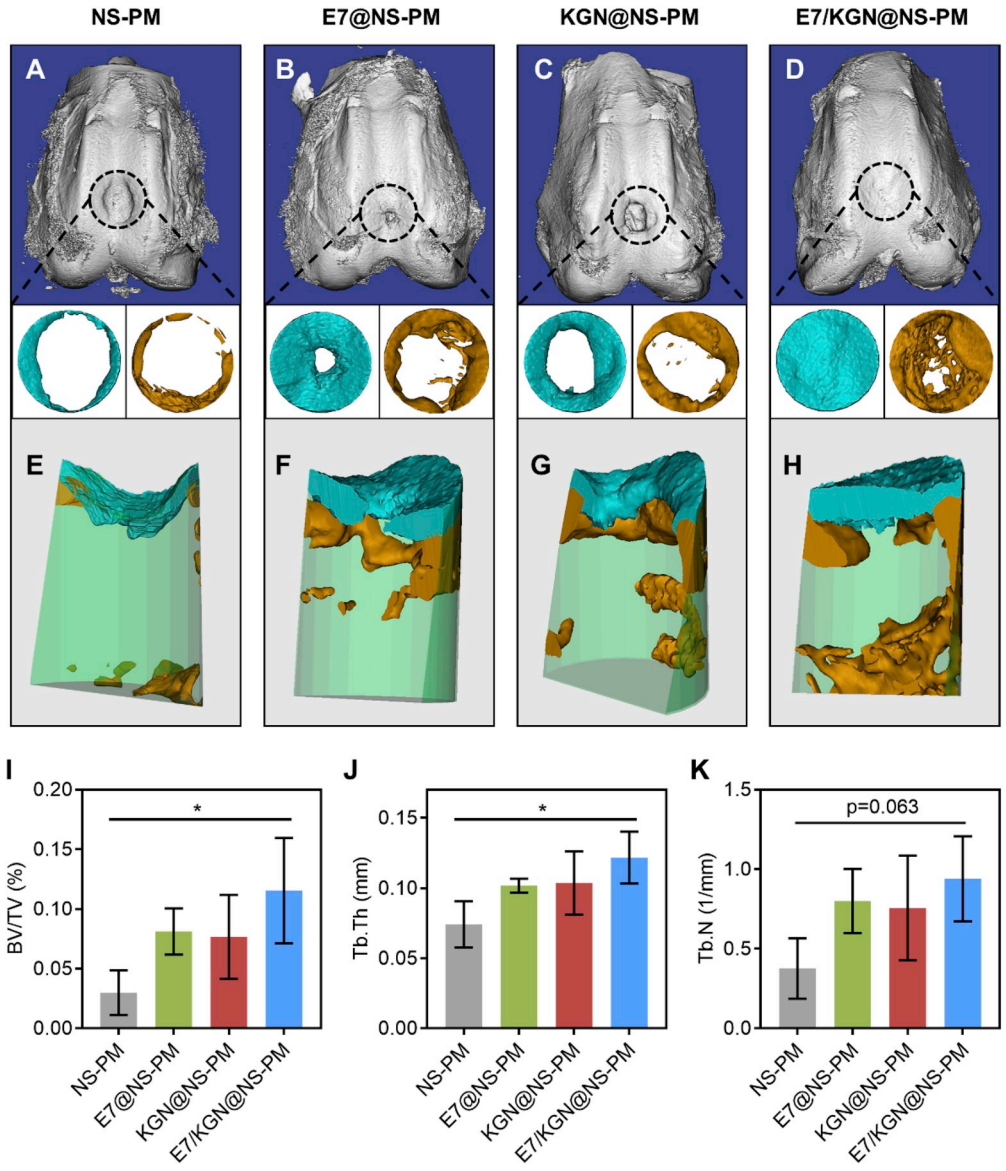

Fig. 7. 3D reconstruction from Micro-CT images of the repaired osteochondral tissue at 12 weeks post-operation. (A-D) Top view. The black circles indicate the original defect borders. Cartilage is denoted in blue and bone is denoted in yellow. (E-H) Cross-sectional view. Cartilage is denoted in blue and bone is denoted in yellow. Quantitative measurements of Micro-CT bone remodeling: (I) BV/TV (%), (J) Tb.Th, and (K) Tb.N. *P < 0.05.

migratory factor E7 can recruit endogenous BMSCs to the defect site, which are the building blocks for subsequent tissue repair [9]. It can be confirmed from our results as only a very small amount of neo-tissues have been formed in the defects without E7 presentation (NS-PM, KGN@NS-PM), indicative of lack of cells. We noticed that the SF nanosphere matrix loaded with E7 alone (E7@NS-PM) indeed induced more abundant generation of neo-tissues as compared to the matrices without E7 loading (NS-PM and KGN@NS-PM). However, the repaired tissue in the E7@NS-PM group was mostly immature fibrous tissue as shown by the histological staining (Fig. 8B and F). In contrast, considerable hyaline cartilage-like tissue was generated in the E7/KGN@NS-PM treated defects (Figs. 8D, 8H, 9D, 9H). Such enhanced repair efficacy is mostly attributed to the sustained delivery of KGN, the pro-chondrogenic molecule, to the cells that have been recruited to the defect site by E7.

Although our prepared SF nanosphere matrix with sequential E7/KGN release substantially improved the regeneration of osteochondral defects, the regenerated tissue was still inferior to normal hyaline cartilage, which indicates that the scaffold needs to be further optimized to achieve better repair efficacy. We found that in most repaired samples, the SF porous matrices were not adequately degraded. Scaffold degradation rate slower than tissue regeneration has been shown to impede neo-tissue ingrowth [44]. The degradability of the SF matrix can be optimized by changing the concentration or degree of crosslinking of the porous matrix, or using more degradable formats such as SF hydrogels or electrospun fibers, to coordinate the repair process [45–47].

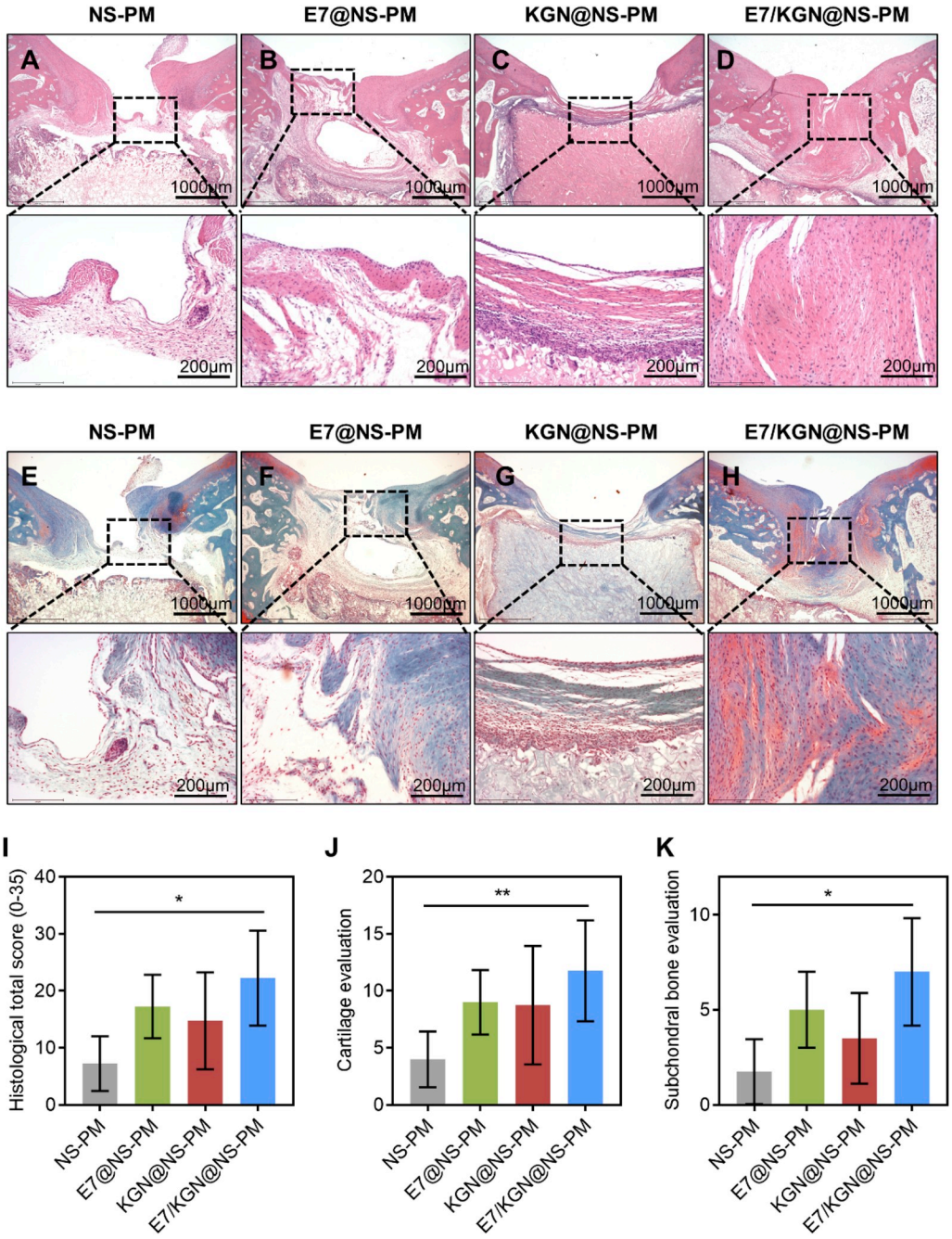

Fig. 8. (A-D) H&E staining images and (E-H) Safranine-O staining images of the repaired osteochondral tissue at 12 weeks post-operation. The lower panels represent higher magnification images of the corresponding black boxes in the upper panel. Scale bars = 1000 μm in the upper panel and 200 μm in the lower panel. (I) Histological evaluation according to the established histological scoring system. (J) Histological evaluation of repaired cartilage according to the cartilage sub-scores of the histological scoring system. (K) Histological evaluation of repaired subchondral bone according to the subchondral bone sub-scores of the histological scoring system. *P < 0.05, **P < 0.01.

Furthermore, other combinations of pro-migratory and pro-differentiation molecules can also be applied to this all-silk-derived sequential delivery system to seek enhanced effects.

4. Conclusions

In conclusion, this study detailed the development and application of an all-silk-derived functional nanosphere matrix for sequential delivery of E7 and KGN to direct the coordinated phases of osteochondral regeneration. By simply changing the initial SF/PVA concentrations of the nanospheres, this specially designed system offered a rapid initial release of E7 to recruit BMSCs at an early stage, and a relatively slow and sustained release of KGN to induce BMSCs chondrogenesis, thereby enhancing osteochondral regeneration. These results provide a promising tissue engineered-scaffold for clinical treatment of osteochondral defects, and this all-silk-derived sequential biomolecule delivery system may have broad implications for improving the therapeutic efficacy of tissue engineering and regenerative medicine researches.

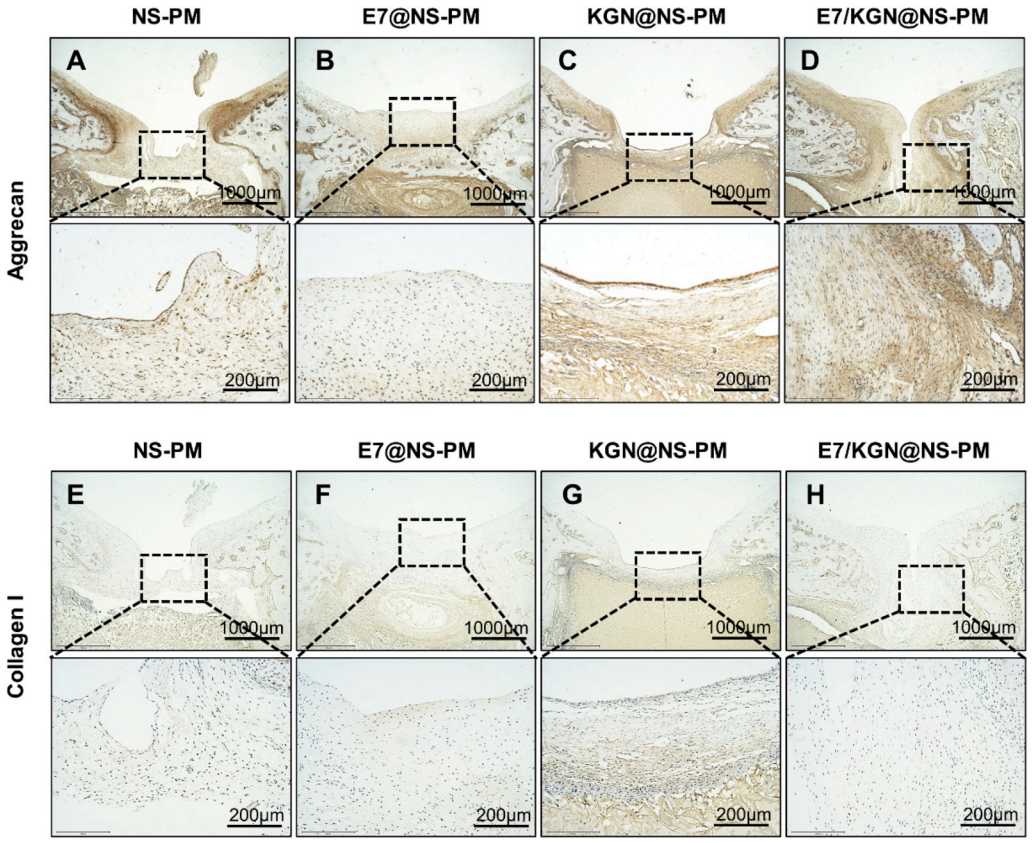

Fig. 9. Immunohistochemical staining for (A-D) Aggrecan and (E-H) Collagen I of the repaired osteochondral tissue at 12 weeks post-operation. The lower panels represent higher magnification images of the corresponding black boxes in the upper panel. Scale bars = 1000 μm in the upper panel and 200 μm in the lower panel.

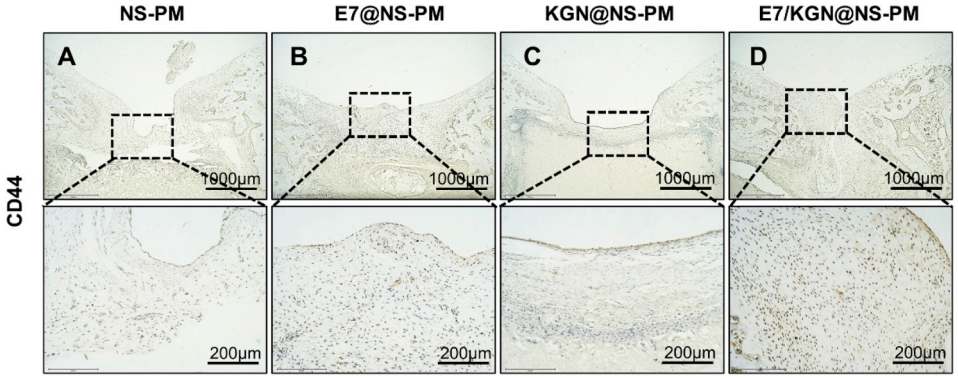

Fig. 10. Immunohistochemical staining for CD44 of the repaired osteochondral tissue at 12 weeks post-operation. The lower panels represent higher magnification images of the corresponding black boxes in the upper panel. Scale bars = 1000 μm in the upper panel and 200 μm in the lower panel.

CRediT authorship contribution statement

Wei Zhang: Conceptualization, Methodology, Data curation, Formal analysis, Funding acquisition, Project administration, Writing - original draft. **Chen Ling:** Data curation, Formal analysis, Investigation, Software. **Aini Zhang:** Data curation, Formal analysis, Investigation. **Haoyang Liu:** Data curation, Formal analysis. **Yujie Jiang:** Data curation, Formal analysis. **Xiaolong Li:** Data curation, Software. **Renwang Sheng:** Data curation, Formal analysis. **Qingqiang Yao:** Funding acquisition, Resources. **Jialin Chen:** Funding acquisition, Writing - review & editing.

Declaration of competing interest

The authors declare that they have no known competing financial interests or personal relationships that could have appeared to influence the work reported in this paper.

Acknowledgements

This work was financially supported by the National Natural Science Foundation of China (81901903, 5171101275, 81771985, 81702205), the Natural Science Foundation of Jiangsu Province (BK20190356, BK20190354), the National Key Research and Development Program of China (2018YFC1105201/204), the Key Research Program of Science & Technology Support Program of Jiangsu Province (BE2016763), the Fundamental Research Funds for the Central Universities (2242019K40127, 2242019K40124), the Scientific Research Staring Foundation for New Scholars of Southeast University (1124007112), and the Funds for Zhishan Young Scholars (Southeast University).

Appendix A. Supplementary data

Supplementary data to this article can be found online at https://doi.org/10.1016/j.bioactmat.2020.05.003.

References

[1] E.R. Vina, C.K. Kwoh, Epidemiology of osteoarthritis: literature update, Curr. Opin. Rheumatol. 30 (2) (2018) 160–167.
[2] E.A. Makris, A.H. Gomoll, K.N. Malizos, J.C. Hu, K.A. Athanasiou, Repair and tissue engineering techniques for articular cartilage, Nat. Rev. Rheumatol. 11 (1) (2015) 21–34.
[3] J. Menetrey, F. Unno-Veith, H. Madry, I. Van Breuseghem, Epidemiology and imaging of the subchondral bone in articular cartilage repair, Knee Surg. Sports Traumatol. Arthrosc. 18 (4) (2010) 463–471.
[4] A.R. Armiento, M.J. Stoddart, M. Alini, D. Eglin, Biomaterials for articular cartilage tissue engineering: learning from biology, Acta Biomater. 65 (2018) 1–20.
[5] S. Pacelli, S. Basu, J. Whitlow, A. Chakravarti, F. Acosta, A. Varshney, S. Modaresi, C. Berkland, A. Paul, Strategies to develop endogenous stem cell-recruiting bioactive materials for tissue repair and regeneration, Adv. Drug Deliv. Rev. 120 (2017) 50–70.
[6] W. Zhang, H.W. Ouyang, C.R. Dass, J.K. Xu, Current research on pharmacologic and regenerative therapies for osteoarthritis, Bone Res. 4 (2016).
[7] F.M. Chen, L.A. Wu, M. Zhang, R. Zhang, H.H. Sun, Homing of endogenous stem/progenitor cells for in situ tissue regeneration: promises, strategies, and translational perspectives, Biomaterials 32 (12) (2011) 3189–3209.
[8] P. Su, Y. Tian, C. Yang, X. Ma, X. Wang, J. Pei, A. Qian, Mesenchymal stem cell migration during bone formation and bone diseases therapy, Int. J. Mol. Sci. 19 (8) (2018).
[9] W.S. Vanden Berg-Foels, In situ tissue regeneration: chemoattractants for endogenous stem cell recruitment, Tissue Eng. B Rev. 20 (1) (2014) 28–39.
[10] S. Camarero-Espinosa, J. Cooper-White, Tailoring biomaterial scaffolds for osteochondral repair, Int. J. Pharm. 523 (2) (2017) 476–489.
[11] M.P. Nikolova, M.S. Chavali, Recent advances in biomaterials for 3D scaffolds: a review, Bioact. Mater. 4 (2019) 271–292.
[12] Y. Chen, T. Wu, S. Huang, C.W. Suen, X. Cheng, J. Li, H. Hou, G. She, H. Zhang, H. Wang, X. Zheng, Z. Zha, Sustained release SDF-1alpha/TGF-beta1-loaded silk fibroin-porous gelatin scaffold promotes cartilage repair, ACS Appl. Mater. Interfaces 11 (16) (2019) 14608–14618.
[13] X. Hu, Y. Wang, Y. Tan, J. Wang, H. Liu, Y. Wang, S. Yang, M. Shi, S. Zhao, Y. Zhang, Q. Yuan, A difunctional regeneration scaffold for knee repair based on aptamer-directed cell recruitment, Adv. Mater. 29 (15) (2017).
[14] A. Hakamivala, L. Shuxin, K. Robinson, Y. Huang, S. Yu, B. Yuan, J. Borrelli Jr., L. Tang, Recruitment of endogenous progenitor cells by erythropoietin loaded particles for in situ cartilage regeneration, Bioact. Mater. 5 (1) (2020) 142–152.
[15] W. Zhang, J.L. Chen, J.D. Tao, C.C. Hu, L.K. Chen, H.S. Zhao, G.W. Xu, B.C. Heng, H.W. Ouyang, The promotion of osteochondral repair by combined intra-articular injection of parathyroid hormone-related protein and implantation of a bi-layer collagen-silk scaffold, Biomaterials 34 (25) (2013) 6046–6057.
[16] J. Fischer, M. Ortel, S. Hagmann, A. Hoeflich, W. Richter, Role of PTHrP(1-34) pulse frequency versus pulse duration to enhance mesenchymal stromal cell chondrogenesis, J. Cell. Physiol. 231 (12) (2016) 2673–2681.
[17] D. Barati, S.R.P. Shariati, S. Moeinzadeh, J.M. Melero-Martin, A. Khademhosseini, E. Jabbari, Spatiotemporal release of BMP-2 and VEGF enhances osteogenic and vasculogenic differentiation of human mesenchymal stem cells and endothelial colony-forming cells co-encapsulated in a patterned hydrogel, J. Contr. Release 223 (2016) 126–136.
[18] X. Shen, Y. Zhang, Y. Gu, Y. Xu, Y. Liu, B. Li, L. Chen, Sequential and sustained release of SDF-1 and BMP-2 from silk fibroin-nanohydroxyapatite scaffold for the enhancement of bone regeneration, Biomaterials 106 (2016) 205–216.
[19] F. Qu, J.L. Holloway, J.L. Esterhai, J.A. Burdick, R.L. Mauck, Programmed biomolecule delivery to enable and direct cell migration for connective tissue repair, Nat. Commun. 8 (1) (2017) 1780.
[20] Z. Liu, X. Chen, Z. Zhang, X. Zhang, L. Saunders, Y. Zhou, P.X. Ma, Nanofibrous spongy microspheres to distinctly release miRNA and growth factors to enrich regulatory T cells and rescue periodontal bone loss, ACS Nano 12 (10) (2018) 9785–9799.
[21] P. Yilgor, K. Tuzlakoglu, R.L. Reis, N. Hasirci, V. Hasirci, Incorporation of a sequential BMP-2/BMP-7 delivery system into chitosan-based scaffolds for bone tissue engineering, Biomaterials 30 (21) (2009) 3551–3559.
[22] B. Kundu, R. Rajkhowa, S.C. Kundu, X. Wang, Silk fibroin biomaterials for tissue regenerations, Adv. Drug Deliv. Rev. 65 (4) (2013) 457–470.
[23] W. Huang, S. Ling, C. Li, F.G. Omenetto, D.L. Kaplan, Silkworm silk-based materials and devices generated using bio-nanotechnology, Chem. Soc. Rev. 47 (17) (2018) 6486–6504.
[24] D.N. Rockwood, R.C. Preda, T. Yucel, X. Wang, M.L. Lovett, D.L. Kaplan, Materials fabrication from Bombyx mori silk fibroin, Nat. Protoc. 6 (10) (2011) 1612–1631.
[25] W. Zhang, L.K. Chen, J.L. Chen, L.S. Wang, X.X. Gui, J.S. Ran, G.W. Xu, H.S. Zhao, M.F. Zeng, J.F. Ji, L. Qian, J.D. Zhou, H.W. Ouyang, X.H. Zou, Silk fibroin biomaterial shows safe and effective wound healing in animal models and a randomized controlled clinical trial, Adv. Healthc. Mater. 6 (10) (2017).
[26] X. Wang, E. Wenk, X. Zhang, L. Meinel, G. Vunjak-Novakovic, D.L. Kaplan, Growth factor gradients via microsphere delivery in biopolymer scaffolds for osteochondral tissue engineering, J. Contr. Release 134 (2) (2009) 81–90.
[27] X. Wang, T. Yucel, Q. Lu, X. Hu, D.L. Kaplan, Silk nanospheres and microspheres from silk/pva blend films for drug delivery, Biomaterials 31 (6) (2010) 1025–1035.
[28] H. Huang, X. Zhang, X. Hu, Z. Shao, J. Zhu, L. Dai, Z. Man, L. Yuan, H. Chen, C. Zhou, Y. Ao, A functional biphasic biomaterial homing mesenchymal stem cells for in vivo cartilage regeneration, Biomaterials 35 (36) (2014) 9608–9619.
[29] J. Wu, L. Cao, Y. Liu, A. Zheng, D. Jiao, D. Zeng, X. Wang, D.L. Kaplan, X. Jiang, Functionalization of silk fibroin electrospun scaffolds via BMSC affinity peptide grafting through oxidative self-polymerization of dopamine for bone regeneration, ACS Appl. Mater. Interfaces 11 (9) (2019) 8878–8895.
[30] Z. Shao, X. Zhang, Y. Pi, X. Wang, Z. Jia, J. Zhu, L. Dai, W. Chen, L. Yin, H. Chen, C. Zhou, Y. Ao, Polycaprolactone electrospun mesh conjugated with an MSC affinity peptide for MSC homing in vivo, Biomaterials 33 (12) (2012) 3375–3387.
[31] Q. Meng, Z. Man, L. Dai, H. Huang, X. Zhang, X. Hu, Z. Shao, J. Zhu, J. Zhang, X. Fu, X. Duan, Y. Ao, A composite scaffold of MSC affinity peptide-modified demineralized bone matrix particles and chitosan hydrogel for cartilage regeneration, Sci. Rep. 5 (2015) 17802.
[32] Z. Man, L. Yin, Z. Shao, X. Zhang, X. Hu, J. Zhu, L. Dai, H. Huang, L. Yuan, C. Zhou, H. Chen, Y. Ao, The effects of co-delivery of BMSC-affinity peptide and rhTGF-beta1 from coaxial electrospun scaffolds on chondrogenic differentiation, Biomaterials 35 (19) (2014) 5250–5260.
[33] W. Zhang, C. Ling, H. Liu, A. Zhang, L. Mao, J. Wang, J. Chao, L.J. Backman, Q. Yao, J. Chen, Tannic acid-mediated dual peptide-functionalized scaffolds to direct stem cell behavior and osteochondral regeneration, Chem. Eng. J. 396 (2020) 125232.
[34] X. Li, J. Ding, Z. Zhang, M. Yang, J. Yu, J. Wang, F. Chang, X. Chen, Kartogenin-incorporated thermogel supports stem cells for significant cartilage regeneration, ACS Appl. Mater. Interfaces 8 (8) (2016) 5148–5159.
[35] J. Xu, Q. Feng, S. Lin, W. Yuan, R. Li, J. Li, K. Wei, X. Chen, K. Zhang, Y. Yang, T. Wu, B. Wang, M. Zhu, R. Guo, G. Li, L. Bian, Injectable stem cell-laden supramolecular hydrogels enhance in situ osteochondral regeneration via the sustained co-delivery of hydrophilic and hydrophobic chondrogenic molecules, Biomaterials 210 (2019) 51–61.
[36] G. Cai, W. Liu, Y. He, J. Huang, L. Duan, J. Xiong, L. Liu, D. Wang, Recent advances in kartogenin for cartilage regeneration, J. Drug Target. 27 (1) (2019) 28–32.
[37] G.I. Im, Application of kartogenin for musculoskeletal regeneration, J. Biomed. Mater. Res. 106 (4) (2018) 1141–1148.
[38] M.P. van den Borne, N.J. Raijmakers, J. Vanlauwe, J. Victor, S.N. de Jong, J. Bellemans, D.B. Saris, S. International, Cartilage repair, international cartilage repair society (ICRS) and oswestry macroscopic cartilage evaluation scores validated for use in autologous chondrocyte implantation (ACI) and microfracture, Osteoarthritis Cartilage 15 (12) (2007) 1397–1402.
[39] Y. Jiang, L. Chen, S. Zhang, T. Tong, W. Zhang, W. Liu, G. Xu, R.S. Tuan, B.C. Heng, R. Crawford, Y. Xiao, H.W. Ouyang, Incorporation of bioactive polyvinylpyrrolidone-iodine within bilayered collagen scaffolds enhances the differentiation and subchondral osteogenesis of mesenchymal stem cells, Acta Biomater. 9 (9) (2013) 8089–8098.
[40] D.Q. Shi, X.Q. Xu, Y.Q. Ye, K. Song, Y.X. Cheng, J. Di, Q.Y. Hu, J.X. Li, H.X. Ju, Q. Jiang, Z. Gu, Photo-cross-linked scaffold with kartogenin-encapsulated nanoparticles for cartilage regeneration, ACS Nano 10 (1) (2016) 1292–1299.
[41] B. Almeida, Y. Wang, A. Shukla, Effects of nanoparticle properties on kartogenin delivery and interactions with mesenchymal stem cells, Ann. Biomed. Eng. (2019).
[42] Y. Huang, H. Yu, C. Xiao, pH-sensitive cationic guar gum/poly (acrylic acid) polyelectrolyte hydrogels: swelling and in vitro drug release, Carbohydr. Polym. 69 (4) (2007) 774–783.
[43] S.A. Lietman, S. Miyamoto, P.R. Brown, N. Inoue, A.H. Reddi, The temporal sequence of spontaneous repair of osteochondral defects in the knees of rabbits is dependent on the geometry of the defect, J. Bone Joint Surg. Br. 84 (4) (2002) 600–606.
[44] H. Zhang, L. Zhou, W. Zhang, Control of scaffold degradation in tissue engineering: a review, Tissue Eng. B Rev. 20 (5) (2014) 492–502.
[45] Q. Lu, B. Zhang, M. Li, B. Zuo, D.L. Kaplan, Y. Huang, H. Zhu, Degradation mechanism and control of silk fibroin, Biomacromolecules 12 (4) (2011) 1080–1086.
[46] X. Wang, J.A. Kluge, G.G. Leisk, D.L. Kaplan, Sonication-induced gelation of silk fibroin for cell encapsulation, Biomaterials 29 (8) (2008) 1054–1064.
[47] J. Zhou, C. Cao, X. Ma, L. Hu, L. Chen, C. Wang, In vitro and in vivo degradation behavior of aqueous-derived electrospun silk fibroin scaffolds, Polym. Degrad. Stabil. 95 (9) (2010) 1679–1685.